

# 19 Chebyshev Expansion Techniques

Alexander Weiße and Holger Fehske

Institut für Physik, Universität Greifswald, 17487 Greifswald, Germany

With the Lanczos and the Jacobi-Davidson algorithm we are able to calculate a few of the many eigenstates of a sparse matrix. However, it is hardly feasible to calculate all eigenstates of matrices with dimensions larger than a million, not to speak of dimensions like  $10^9$ . Nevertheless, we are interested in dynamic correlation functions and finite temperature properties, which depend on the complete spectrum of the Hamiltonian.

In this chapter we introduce the Kernel Polynomial Method (KPM), a numerical approach that on the basis of Chebyshev expansion allows a very precise calculation of the spectral properties of large sparse matrices and of the static and dynamic correlation functions, which depend on them. In addition, we show how the KPM successfully competes against the very popular Lanczos Recursion and Maximum Entropy Method and can be easily embedded into other numerical techniques, such as Cluster Perturbation Theory or Monte Carlo simulation. Characterized by a resource consumption that scales linearly with the problem dimension the KPM enjoyed growing popularity over the last decade and found broad application not only in physics (for a recent more detailed review see [1]).

## 19.1 Chebyshev Expansion and Kernel Polynomial Approximation

### 19.1.1 General Aspects

Let us first recall the basic properties of expansions in orthogonal polynomials and of Chebyshev expansion in particular. Given a positive weight function  $w(x)$  defined on the interval  $[a, b]$  we can introduce a scalar product

$$\langle f|g \rangle = \int_a^b w(x) f(x) g(x) dx \quad (19.1)$$

between two integrable functions  $f, g: [a, b] \rightarrow \mathbb{R}$ . With respect to this scalar product there exists a complete set of polynomials  $p_n(x)$ , which fulfil the orthogonality relations  $\langle p_n | p_m \rangle = \delta_{n,m} / h_n$ , where  $h_n = 1 / \langle p_n | p_n \rangle$  denotes the inverse of the squared norm of  $p_n(x)$ . These orthogonality relations allow for an easy expansion

of a given function  $f(x)$  in terms of the  $p_n(x)$ , since the expansion coefficients are proportional to the scalar products of  $f$  and  $p_n$ ,

$$f(x) = \sum_{n=0}^{\infty} \alpha_n p_n(x) \tag{19.2}$$

with  $\alpha_n = \langle p_n | f \rangle h_n$ .

In general, all types of orthogonal polynomials can be used for such an expansion and for the KPM approach which we discuss in this chapter (see e.g. [2]). However, as we frequently observe whenever we work with polynomial expansions [3], Chebyshev polynomials [4, 5] of first and second kind turn out to be the best choice for most applications, mainly due to the good convergence properties of the corresponding series and the close relation to Fourier transform [6, 7]. The latter is also an important prerequisite for the derivation of optimal kernels (see below), which are required for the regularization of finite-order expansions, and which so far have not been derived for other sets of orthogonal polynomials.

There are two sets of Chebyshev polynomials, both defined on the interval  $[a, b] = [-1, 1]$ : The weight function  $w(x) = (\pi\sqrt{1-x^2})^{-1}$  yields the polynomials of first kind,  $T_n$ , and the weight function  $w(x) = \pi\sqrt{1-x^2}$  those of second kind,  $U_n$ . In what follows we focus on the  $T_n = \cos(n \arccos(x))$ , which after substituting  $x = \cos(\varphi)$  can be shown to fulfil the orthogonality relation  $\langle T_n | T_m \rangle = \delta_{n,m} (1 + \delta_{n,0})/2$ . Moreover, we can easily prove the recursion relation

$$T_{m+1}(x) = 2x T_m(x) - T_{m-1}(x) , \tag{19.3}$$

and the addition formula

$$2T_m(x)T_n(x) = T_{m+n}(x) + T_{m-n}(x) , \tag{19.4}$$

where  $T_{-n}(x) = T_n(x)$  and  $T_0(x) = 1$ .

Expanding a function  $f$  in the standard way of (19.2), the determination of the coefficients  $\langle T_n | f \rangle$  requires integrations over the weight function  $w(x)$ , see (19.1). In practical applications to matrix problems this prohibits a simple iterative scheme, but a solution follows from a slight rearrangement of the expansion, namely

$$f(x) = \frac{1}{\pi\sqrt{1-x^2}} \left( \mu_0 + 2 \sum_{n=1}^{\infty} \mu_n T_n(x) \right) \tag{19.5}$$

with the modified coefficients (moments)

$$\mu_n = \int_{-1}^1 f(x) T_n(x) dx . \tag{19.6}$$

These two equations are the general basis for the Chebyshev expansion. In the remaining sections we will explain how to translate physical quantities into polynomial expansions of the form of (19.5), how to calculate the moments  $\mu_n$  in practice, and how to improve the convergence of the approach.

### 19.1.2 Calculation of Moments

A common feature of basically all Chebyshev expansions is the requirement for a rescaling of the underlying matrix or Hamiltonian  $H$ . While Chebyshev polynomials are defined on the real interval  $[-1, 1]$ , the quantities we are interested in usually depend on the eigenvalues  $\{E_k\}$  of the considered (finite-dimensional) matrix. To fit this spectrum into the interval  $[-1, 1]$  we apply a simple linear transformation to the Hamiltonian and all energy scales,

$$\tilde{H} = \frac{H - b}{a}, \quad \tilde{E} = \frac{E - b}{a}, \quad (19.7)$$

and denote all rescaled quantities with a tilde hereafter. Given the extremal eigenvalues of the Hamiltonian,  $E_{\min}$  and  $E_{\max}$ , which can be calculated, e.g. with the Lanczos algorithm [8], or for which bounds may be known analytically, the scaling factors  $a$  and  $b$  read  $a = (E_{\max} - E_{\min})/(2 - \epsilon)$ ,  $b = (E_{\max} + E_{\min})/2$ . The parameter  $\epsilon$  is a small cut-off introduced to avoid stability problems that arise if the spectrum includes or exceeds the boundaries of the interval  $[-1, 1]$ . It can be fixed, e.g. to  $\epsilon = 0.01$ , or adapted to the resolution of the calculation, which for an expansion of finite order  $N$  is proportional  $1/N$  (see below).

The next similarity of most Chebyshev expansions is the form of the moments, namely their dependence on the matrix or Hamiltonian  $\tilde{H}$ . In general, we find two types of moments: Simple expectation values of Chebyshev polynomials in  $\tilde{H}$ ,

$$\mu_n = \langle \beta | T_n(\tilde{H}) | \alpha \rangle, \quad (19.8)$$

where  $|\alpha\rangle$  and  $|\beta\rangle$  are certain states of the system, or traces over such polynomials and a given operator  $A$ ,

$$\mu_n = \text{Tr}[A T_n(\tilde{H})]. \quad (19.9)$$

Handling the first case is rather straightforward. Starting from the state  $|\alpha\rangle$  we can iteratively construct the states  $|\alpha_n\rangle = T_n(\tilde{H})|\alpha\rangle$  by using the recursion relations for the  $T_n$  (see (19.3)),

$$|\alpha_0\rangle = |\alpha\rangle, \quad |\alpha_1\rangle = \tilde{H}|\alpha_0\rangle, \quad |\alpha_{n+1}\rangle = 2\tilde{H}|\alpha_n\rangle - |\alpha_{n-1}\rangle. \quad (19.10)$$

Scalar products with  $|\beta\rangle$  then directly yield  $\mu_n = \langle \beta | \alpha_n \rangle$ .

The iterative calculation of the moments, in particular the application of  $\tilde{H}$  to the state  $|\alpha_n\rangle$ , represents the most time consuming part of the whole expansion approach and determines its performance. If  $\tilde{H}$  is a sparse matrix of dimension  $D$  the MVM is an order  $O(D)$  process and the calculation of  $N$  moments therefore requires  $O(ND)$  operations and time. The memory consumption depends on the implementation. For moderate problem dimension we can store the matrix and, in addition, need memory for two vectors of dimension  $D$ . For very large  $D$  the matrix certainly does not fit into the memory and has to be reconstructed on-the-fly in each iteration or retrieved from disc. The two vectors then determine the memory

consumption of the calculation. Overall, the resource consumption of the moment iteration is similar or even slightly better than that of the Lanczos algorithm, which requires a few more vector operations (see our comparison in Sect. 19.3). In contrast to Lanczos, Chebyshev iteration is completely stable and can be carried out to arbitrary high order.

The moment iteration can be simplified even further, if  $|\beta\rangle = |\alpha\rangle$ . In this case the product relation (19.4) allows for the calculation of two moments from each new  $|\alpha_n\rangle$

$$\mu_{2n} = 2\langle\alpha_n|\alpha_n\rangle - \mu_0, \quad \mu_{2n+1} = 2\langle\alpha_{n+1}|\alpha_n\rangle - \mu_1, \quad (19.11)$$

which is equivalent to two moments per MVM. The numerical effort for  $N$  moments is thus reduced by a factor of two. In addition, like many other numerical approaches KPM benefits considerably from the use of symmetries that reduce the Hilbert space dimension.

The second case where the moments depend on a trace over the whole Hilbert space, at first glance, looks far more complicated. Based on the previous considerations we would estimate the numerical effort to be proportional to  $D^2$ , because the iteration needs to be repeated for all  $D$  states of a given basis. It turns out, however, that extremely good approximations of the moments can be obtained with a much simpler approach: The stochastic evaluation of the trace [2, 9, 10], i.e., an estimate of  $\mu_n$  based on the average over only a small number  $R \ll D$  of randomly chosen states  $|r\rangle$

$$\mu_n = \text{Tr}[A T_n(\tilde{H})] \approx \frac{1}{R} \sum_{r=0}^{R-1} \langle r|A T_n(\tilde{H})|r\rangle. \quad (19.12)$$

The number of random states  $R$  does not scale with  $D$ . It can be kept constant or even reduced with increasing  $D$ . To understand this, let us consider the convergence properties of the above estimate. Given an arbitrary basis  $\{|i\rangle\}$  and a set of independent identically distributed random variables  $\xi_{ri} \in \mathbb{C}$ , which in terms of the statistical average  $\langle\langle \dots \rangle\rangle$  fulfil

$$\langle\langle \xi_{ri} \rangle\rangle = 0, \quad \langle\langle \xi_{ri} \xi_{r'j} \rangle\rangle = 0, \quad \langle\langle \xi_{ri}^* \xi_{r'j} \rangle\rangle = \delta_{rr'} \delta_{ij}, \quad (19.13)$$

a random vector is defined through  $|r\rangle = \sum_{i=0}^{D-1} \xi_{ri} |i\rangle$ . We can now calculate the statistical expectation value of the trace estimate  $\Theta = \frac{1}{R} \sum_{r=0}^{R-1} \langle r|B|r\rangle$  for some Hermitian operator  $B$  with matrix elements  $B_{ij} = \langle i|B|j\rangle$ , and indeed find,

$$\langle\langle \Theta \rangle\rangle = \langle\langle \frac{1}{R} \sum_{r=0}^{R-1} \langle r|B|r\rangle \rangle\rangle = \frac{1}{R} \sum_{r=0}^{R-1} \sum_{i,j=0}^{D-1} \langle\langle \xi_{ri}^* \xi_{rj} \rangle\rangle B_{ij} = \sum_{i=0}^{D-1} B_{ii} = \text{Tr}(B). \quad (19.14)$$

Of course, this only shows that we obtain the correct result on average. To assess the associated error we also need to study the fluctuation of  $\Theta$ , which is characterized by  $(\delta\Theta)^2 = \langle\langle \Theta^2 \rangle\rangle - \langle\langle \Theta \rangle\rangle^2$ . Evaluating  $\langle\langle \Theta^2 \rangle\rangle$ , we get for the fluctuation

$$(\delta\Theta)^2 = \frac{1}{R} \left[ \text{Tr}(B^2) + (\langle\langle |\xi_{ri}|^4 \rangle\rangle - 2) \sum_{j=0}^{D-1} B_{jj}^2 \right]. \quad (19.15)$$

The trace of  $B^2$  will usually be of order  $O(D)$ , and the relative error of the trace estimate,  $\delta\Theta/\Theta$ , is thus of order  $O(1/\sqrt{RD})$ . It is this favorable behavior, which ensures the convergence of the stochastic approach, and which was the basis for our initial statement that the number of random states  $R \ll D$  can be kept small or even be reduced with the problem dimension  $D$ .

### 19.1.3 Damping of Gibbs Oscillations – Kernel Polynomials

In the preceding sections we introduced the basic ideas underlying the expansion of a function  $f(x)$  in an infinite series of Chebyshev polynomials, and gave a few hints for the numerical calculation of the expansion coefficients  $\mu_n$ . For a numerical approach, however, the total number of moments will remain finite, and we have to look for the best (uniform) approximation to  $f(x)$  by polynomials of given maximal degree  $N$ . Introducing the concept of kernels, we will investigate and optimize the convergence properties of the mapping  $f(x) \rightarrow f_{\text{KPM}}(x)$  from the considered function  $f(x)$  to our approximation  $f_{\text{KPM}}(x)$ .

Experience shows that a simple truncation of an infinite series,

$$f(x) \approx \frac{1}{\pi\sqrt{1-x^2}} \left( \mu_0 + 2 \sum_{n=1}^{N-1} \mu_n T_n(x) \right), \quad (19.16)$$

leads to poor precision and fluctuations – also known as Gibbs oscillations – near points where the function  $f(x)$  is not continuously differentiable. The situation is even worse for discontinuities or singularities of  $f(x)$ , as we illustrate in Fig. 19.1. A common procedure to damp these oscillations relies on an appropriate modification of the expansion coefficients,  $\mu_n \rightarrow g_n\mu_n$ , which depends on the order of the approximation  $N$ ,

$$f_{\text{KPM}}(x) = \frac{1}{\pi\sqrt{1-x^2}} \left( g_0\mu_0 + 2 \sum_{n=1}^{N-1} g_n\mu_n T_n(x) \right). \quad (19.17)$$

This truncation of the infinite series to order  $N$  together with the corresponding modification of the coefficients is equivalent to the convolution of  $f(x)$  with a kernel  $K_N(x, y)$ ,

$$f_{\text{KPM}}(x) = \int_{-1}^1 \pi\sqrt{1-y^2} K_N(x, y) f(y) dy, \quad (19.18)$$

where

$$K_N(x, y) = g_0\phi_0(x)\phi_0(y) + 2 \sum_{n=1}^{N-1} g_n\phi_n(x)\phi_n(y), \quad (19.19)$$

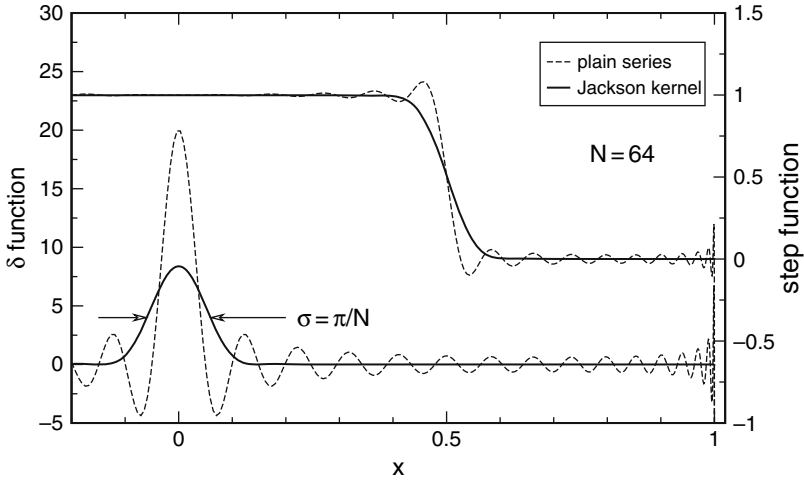


**Fig. 19.1.** Order  $N = 64$  expansions of  $\delta(x)$  and a step. Whereas the truncated series (Dirichlet kernel) strongly oscillate, the Jackson results smoothly converge to the expanded functions

and  $\phi_n(x) = T_n(x)/(\pi\sqrt{1-x^2})$ . This way the problem translates into finding an optimal kernel  $K_N(x, y)$ , i.e., coefficients  $g_n$ . Clearly the notion of *optimal* depends on the application considered.

The standard truncated series corresponds to the choice  $g_n^D = 1$ , which leads to what is usually called the Dirichlet kernel,

$$K_N^D(x, y) = [\phi_N(x)\phi_{N-1}(y) - \phi_{N-1}(x)\phi_N(y)]/(x - y). \tag{19.20}$$

An approximation based on this kernel for  $N \rightarrow \infty$  converges within the integral norm  $\|f\|_2 = \sqrt{\langle f|f \rangle}$ , i.e. we have

$$\|f - f_{\text{KPM}}\|_2 \xrightarrow{N \rightarrow \infty} 0. \tag{19.21}$$

This is, of course, not particularly restrictive and leads to the disadvantages we mentioned earlier.

A much better criterion would be uniform convergence,

$$\|f - f_{\text{KPM}}\|_\infty = \max_{-1 < x < 1} |f(x) - f_{\text{KPM}}(x)| \xrightarrow{N \rightarrow \infty} 0, \tag{19.22}$$

and, indeed, this can be achieved for continuous functions  $f$  under very general conditions. Specifically, it suffices to demand that:

- (i) The kernel is positive:  $K_N(x, y) > 0 \forall x, y \in [-1, 1]$ .
- (ii) The kernel is normalized,  $\int_{-1}^1 K(x, y) dx = \phi_0(y)$ , which is equivalent to  $g_0 = 1$ .
- (iii) The second coefficient  $g_1$  approaches 1 as  $N \rightarrow \infty$ .

The conditions (i) and (ii) are very useful for practical applications: The first ensures that approximations of positive quantities become positive, the second conserves the integral of the expanded function,  $\int_{-1}^1 f_{\text{KPM}}(x) dx = \int_{-1}^1 f(x) dx$ . Applying the kernel, for example, to a density of states thus yields an approximation which is strictly positive and normalized.

The simplest kernel which fulfils all three conditions is the Fejér kernel [11],

$$K_N^F(x, y) = \frac{1}{N} \sum_{\nu=1}^N K_\nu^D(x, y), \tag{19.23}$$

i.e.,  $g_n^F = 1 - n/N$ , which is the arithmetic mean of all Dirichlet approximations of order less or equal  $N$ . However, with the coefficients  $g_n^F$  of the Fejér kernel we have not fully exhausted the freedom offered by the above conditions. We can hope to further improve the kernel by optimizing the  $g_n$  in some sense, which will lead us to recover old results by Jackson [12, 13]. In particular, let us tighten the third condition by demanding that the kernel has optimal resolution in the sense that

$$Q := \int_{-1}^1 \int_{-1}^1 (x - y)^2 K_N(x, y) dx dy \tag{19.24}$$

is minimal. Since  $K_N(x, y)$  is peaked at  $x = y$ ,  $Q$  is basically the squared width of this peak and a measure for the resolution of the kernel. For sufficiently smooth functions this more stringent condition will minimize the error  $\|f - f_{\text{KPM}}\|_\infty$ , and in all other cases lead to optimal resolution and smallest broadening of sharp features.

The optimization [1, 12, 13] leads to a kernel first described by Jackson,  $K_N^J(x, y)$  with

$$g_n^J = \frac{(N - n + 1) \cos(\pi n / (N + 1)) + \sin(\pi n / (N + 1)) \cot(\pi / (N + 1))}{N + 1}, \tag{19.25}$$

which yields the minimal value of  $Q$ ,

$$Q_{\min} = 1 - \cos \frac{\pi}{N + 1} \simeq \frac{1}{2} \left( \frac{\pi}{N} \right)^2. \tag{19.26}$$

This shows that for large  $N$  the resolution  $\sqrt{Q}$  of the new kernel is proportional to  $1/N$ .

The quantity  $\sqrt{Q_{\min}}$  obtained in (19.26) is mainly a measure for the spread of the kernel  $K_N^J(x, y)$  in the  $x$ - $y$ -plane. For practical calculations, which may also involve singular functions, it is reasonable to ask for the broadening of a  $\delta$ -function under convolution with the kernel,  $\delta_{\text{KPM}}(x - a) = g_0 \phi_0(x) T_0(a) + 2 \sum_{n=1}^{N-1} g_n \phi_n(x) T_n(a)$ . It can be characterized by the variance  $\sigma^2 = \langle\langle x^2 \rangle\rangle - \langle\langle x \rangle\rangle^2$ , which after a short calculation is found to be

$$\sigma^2 \simeq \left( \frac{\pi}{N} \right)^2 \left( 1 - a^2 + \frac{4a^2 - 3}{N} \right). \tag{19.27}$$

Using the Jackson kernel, an order  $N$  expansion of a  $\delta$ -function at  $x = 0$  thus results in a broadened peak of width  $\sigma = \pi/N$ , whereas close to the boundaries,  $a = \pm 1$ , we find  $\sigma = \pi/N^{3/2}$ . It turns out that this peak is a good approximation to a Gaussian (see Fig. 19.1),

$$\delta_{\text{KPM}}^{\text{J}}(x) \approx \frac{1}{\sqrt{2\pi\sigma^2}} e^{-x^2/(2\sigma^2)}. \tag{19.28}$$

The Jackson kernel is the best choice for most of the applications we discuss below. In some situations, however, special analytical properties of the expanded functions become important, which only other kernels can account for. Single-particle Green functions that appear in the Cluster Perturbation Theory (see Sect. 19.3), are an example. Considering the imaginary part of the Plemelj-Dirac formula,  $\lim_{\epsilon \rightarrow 0} 1/(x + i\epsilon) = \mathcal{P}(1/x) - i\pi\delta(x)$  (here  $\mathcal{P}$  denotes the principal value), which frequently occurs in connection with Green functions, the  $\delta$ -function on the right hand side is approached in terms of a Lorentz curve,

$$\delta(x) = -\frac{1}{\pi} \lim_{\epsilon \rightarrow 0} \text{Im} \frac{1}{x + i\epsilon} = \lim_{\epsilon \rightarrow 0} \frac{\epsilon}{\pi(x^2 + \epsilon^2)}. \tag{19.29}$$

It has a different and broader shape compared to the approximations of  $\delta(x)$  we get with the Jackson kernel. We can construct [1] a positive normalized kernel which perfectly mimics the above behavior, and consequently call it the Lorentz kernel  $K_N^{\text{L}}(x, y)$  with

$$g_n^{\text{L}} = \frac{\sinh[\lambda(1 - n/N)]}{\sinh(\lambda)}. \tag{19.30}$$

Here,  $\lambda$  is a free parameter which as a compromise between good resolution and sufficient damping of the Gibbs oscillations we empirically choose in order of four. It is related to the  $\epsilon$ -parameter of the Lorentz curve, i.e. to its resolution, via  $\epsilon = \lambda/N$ . Note also, that in the limit  $\lambda \rightarrow 0$  we recover the Fejér kernel  $K_N^{\text{F}}(x, y)$ , suggesting that both kernels share many of their convergence properties.

### 19.1.4 Multi-Dimensional Expansions

For the calculation of finite-temperature dynamical correlation functions we will later need expansions of functions of two variables. Let us therefore briefly comment on the generalization of the above considerations to  $d$ -dimensional space, which is easily obtained by extending the scalar products  $\langle \cdot | \cdot \rangle$  to functions  $f, g : [-1, 1]^d \rightarrow \mathbb{R}$ . As in the one-dimensional case, a simple truncation of the infinite series will lead to Gibbs oscillations and poor convergence. Fortunately, we can easily generalize our results for kernel approximations. In particular, we find that the extended kernel  $K_N(\mathbf{x}, \mathbf{y}) = \prod_{j=1}^d K_N(x_j, y_j)$  maps an infinite series onto a truncated series

$$f_{\text{KPM}}(\mathbf{x}) = \frac{\sum_{\mathbf{n}=0}^{N-1} \mu_{\mathbf{n}} h_{\mathbf{n}} \prod_{j=1}^d g_{n_j} T_{n_j}(x_j)}{\prod_{j=1}^d \pi \sqrt{1 - x_j^2}}, \tag{19.31}$$

where we can take the  $g_n$  of any of the previously discussed kernels. If we use the  $g_n^J$  of the Jackson kernel,  $K_N^J(\mathbf{x}, \mathbf{y})$  fulfils generalizations of our conditions for an optimal kernel, namely

- (i)  $K_N^J(\mathbf{x}, \mathbf{y})$  is positive  $\forall \mathbf{x}, \mathbf{y} \in [-1, 1]^d$ .
- (ii)  $K_N^J(\mathbf{x}, \mathbf{y})$  is normalized with

$$\int_{-1}^1 \cdots \int_{-1}^1 f_{\text{KPM}}(\mathbf{x}) \, dx_1 \dots dx_d = \int_{-1}^1 \cdots \int_{-1}^1 f(\mathbf{x}) \, dx_1 \dots dx_d. \quad (19.32)$$

- (iii)  $K_N^J(\mathbf{x}, \mathbf{y})$  has optimal resolution in the sense that

$$Q = \int_{-1}^1 \cdots \int_{-1}^1 (\mathbf{x} - \mathbf{y})^2 K_N(\mathbf{x}, \mathbf{y}) \, dx_1 \dots dx_d \, dy_1 \dots dy_d = d(g_0 - g_1) \quad (19.33)$$

is minimal.

Note that for simplicity the order of the expansion,  $N$ , was chosen to be the same for all spatial directions. Of course, we could also define more general kernels,  $K_N(\mathbf{x}, \mathbf{y}) = \prod_{j=1}^d K_{N_j}(x_j, y_j)$ , where the vector  $N$  denotes the orders of expansion for the different spatial directions.

### 19.1.5 Numerical Implementation

Having discussed the theory behind Chebyshev expansion, the calculation of moments, and the various kernel approximations, let us now come to the practical issues of the implementation of KPM, namely to the reconstruction of the expanded function  $f(x)$  from its moments  $\mu_n$ . Knowing a finite number  $N$  of coefficients  $\mu_n$ , we usually want to reconstruct  $f(x)$  on a finite set of abscissas  $x_k$ . Naively we could sum up (19.17) separately for each point, thereby making use of the recursion relations for  $T_n$ , i.e.,  $f(x_k) = (g_0 \mu_0 + 2 \sum_{n=1}^{N-1} g_n \mu_n T_n(x_k)) / (\pi \sqrt{1 - x_k^2})$ . For a set  $\{x_k\}$  containing  $\tilde{N}$  points these summations would require of the order of  $N\tilde{N}$  operations. We can do much better, remembering the definition  $T_n(x) = \cos(n \arccos(x))$  and the close relation between KPM and Fourier expansion: First, we may introduce the short-hand notation  $\tilde{\mu}_n = \mu_n g_n$  for the kernel improved moments. Second and more important, we make a special choice for our data points,

$$x_k = \cos \frac{\pi(k + 1/2)}{\tilde{N}} \quad (19.34)$$

with  $k = 0, \dots, (\tilde{N} - 1)$ , which coincides with the abscissas of Chebyshev numerical integration [4]. The number  $\tilde{N}$  of points in the set  $\{x_k\}$  is not necessarily the same as the number of moments  $N$ . Usually we will consider  $\tilde{N} \geq N$  and a

reasonable choice is, e.g.  $\tilde{N} = 2N$ . All values  $f(x_k)$  can now be obtained through a discrete cosine transform,

$$\gamma_k = \pi \sqrt{1 - x_k^2} f(x_k) = \tilde{\mu}_0 + 2 \sum_{n=1}^{N-1} \tilde{\mu}_n \cos\left(\frac{\pi n(k + 1/2)}{\tilde{N}}\right) \quad (19.35)$$

which allows for the use of divide-and-conquer type algorithms that require only  $\tilde{N} \log \tilde{N}$  operations – a clear advantage over the above estimate  $N\tilde{N}$ .

Routines for fast discrete cosine transform are implemented in many mathematical libraries or Fast Fourier Transform (FFT) packages, for instance, in FFTW [14, 15] that ships with most Linux distributions. If no direct implementation is at hand we may also use fast discrete Fourier transform. With

$$\lambda_n = \begin{cases} (2 - \delta_{n,0}) \tilde{\mu}_n e^{i\pi n/(2\tilde{N})} & 0 < n < N \\ 0 & \text{otherwise} \end{cases} \quad (19.36)$$

and the standard definition of discrete Fourier transform,

$$\tilde{\lambda}_k = \sum_{n=0}^{\tilde{N}-1} \lambda_n e^{2\pi i n k / \tilde{N}}, \quad (19.37)$$

after some reordering we find for an even number of data points

$$\gamma_{2j} = \text{Re}(\tilde{\lambda}_j), \quad \gamma_{2j+1} = \text{Re}(\tilde{\lambda}_{\tilde{N}-1-j}), \quad (19.38)$$

with  $j = 0, \dots, \tilde{N}/2 - 1$ . If we need only a discrete cosine transform this setup is not optimal, as it makes no use of the imaginary part which the complex FFT calculates. It turns out, however, that the wasted imaginary part is exactly what we need when we later calculate Green functions and other complex quantities, i.e., we can use the setup

$$\gamma_{2j} = \tilde{\lambda}_j, \quad \gamma_{2j+1} = \tilde{\lambda}_{\tilde{N}-1-j}^*, \quad (19.39)$$

to evaluate (19.58).

## 19.2 Applications of the Kernel Polynomial Method

Having described the mathematical background of the KPM, we are now in the position to present practical applications of the approach. KPM can be used whenever we are interested in the spectral properties of large matrices or in correlation functions that can be expressed through the eigenstates of such matrices. In what follows, we try to cover all types of accessible quantities, focusing on lattice models from solid state physics.

### 19.2.1 Density of States

The first and basic application of Chebyshev expansion and KPM is the calculation of the spectral density of Hermitian matrices, which could correspond to the densities of states of both interacting or non-interacting quantum models [2, 9, 16, 17]. To be specific, let us consider a  $D$ -dimensional matrix  $M$  with eigenvalues  $E_k$ , whose spectral density is defined as

$$\rho(E) = \frac{1}{D} \sum_{k=0}^{D-1} \delta(E - E_k). \quad (19.40)$$

As described earlier, the expansion of  $\rho(E)$  in terms of Chebyshev polynomials requires a rescaling of  $M \rightarrow \tilde{M}$ , such that the spectrum of  $\tilde{M} = (M - b)/a$  fits the interval  $[-1, 1]$ . Given the eigenvalues  $\tilde{E}_k$  of  $\tilde{M}$  the rescaled density  $\tilde{\rho}(\tilde{E})$  reads  $\tilde{\rho}(\tilde{E}) = D^{-1} \sum_{k=0}^{D-1} \delta(\tilde{E} - \tilde{E}_k)$ , and according to (19.6) the expansion coefficients become

$$\begin{aligned} \mu_n &= \int_{-1}^1 \tilde{\rho}(\tilde{E}) T_n(\tilde{E}) d\tilde{E} = \frac{1}{D} \sum_{k=0}^{D-1} T_n(\tilde{E}_k) \\ &= \frac{1}{D} \sum_{k=0}^{D-1} \langle k | T_n(\tilde{M}) | k \rangle = \frac{1}{D} \text{Tr}(T_n(\tilde{M})). \end{aligned} \quad (19.41)$$

This is exactly the trace form that we introduced in Sect. 19.1, and we can immediately calculate the  $\mu_n$  using the stochastic techniques described before. Knowing the moments we can reconstruct  $\tilde{\rho}(\tilde{E})$  for the whole range  $[-1, 1]$ , and a final rescaling yields  $\rho(E)$ .

As the first physical example let us consider percolation of non-interacting fermions in disordered solids. The percolation problem is characterized by the interplay of pure classical and quantum effects. Besides the question of finding a percolating path of accessible sites through a given lattice the quantum nature of the electrons imposes further restrictions on the existence of extended states and, consequently, of a finite dc-conductivity. As a particularly simple model describing this situation we consider a tight-binding one-electron Hamiltonian

$$H = \sum_{i=1} \epsilon_i c_i^\dagger c_i - t \sum_{\langle ij \rangle} \left( c_i^\dagger c_j + \text{H.c.} \right) \quad (19.42)$$

on a simple cubic lattice with  $L^3$  sites and random on-site energies  $\epsilon_i$  drawn from the bimodal distribution  $p(\epsilon_i) = p \delta(\epsilon_i - \epsilon_A) + (1 - p) \delta(\epsilon_i - \epsilon_B)$ , also known as the binary alloy model (see Chap. 17). In the limit  $\Delta = (\epsilon_B - \epsilon_A) \rightarrow \infty$  the wavefunction of the  $A$  sub-band vanishes identically on the  $B$ -sites, making them completely inaccessible for the quantum particles. We then arrive at a situation where non-interacting electrons move on a random ensemble of lattice points, which, depending on  $p$ , may span the entire lattice or not. The corresponding Hamiltonian

reads  $H = -t \sum_{\langle ij \rangle \in A} (c_i^\dagger c_j + \text{H.c.})$ , where the summation extends over nearest-neighbor  $A$ -sites only and, without loss of generality,  $\epsilon_A$  is chosen to be zero.

In the theoretical investigation of disordered systems it turned out that distribution functions for the random quantities take the center stage [18, 19]. The distribution  $f(\rho_i(E))$  of the local density of states (LDOS)

$$\rho_i(E) = \sum_{n=1}^N |\psi_n(\mathbf{r}_i)|^2 \delta(E - E_n) \quad (19.43)$$

is particularly suited because  $\rho_i(E)$  measures the local amplitude of the wavefunction at site  $\mathbf{r}_i$ . It therefore contains direct information about the localization properties. In contrast to the (arithmetically averaged) *mean* DOS,  $\rho_{\text{me}}(E) = \langle \rho_i(E) \rangle$ , the LDOS becomes critical at the localization transition [20, 21]. Therefore the (geometrically averaged) so-called *typical* DOS,  $\rho_{\text{ty}}(E) = \exp(\langle \ln \rho_i(E) \rangle)$ , is frequently used to monitor the transition from extended to localized states. The typical DOS puts sufficient weight on small values of  $\rho_i$  and a comparison to  $\rho_{\text{me}}(E)$  allows to detect the localization transition.

Using the KPM the LDOS can be easily calculated for a large number of samples,  $K_r$ , and sites,  $K_s$ . The mean and typical DOS are then simply obtained from

$$\rho_{\text{me}}(E) = \frac{1}{K_r K_s} \sum_{k=1}^{K_r} \sum_{i=1}^{K_s} \rho_i(E), \quad \rho_{\text{ty}}(E) = \exp \left[ \frac{1}{K_r K_s} \sum_{k=1}^{K_r} \sum_{i=1}^{K_s} \ln(\rho_i(E)) \right], \quad (19.44)$$

respectively. We classify a state at energy  $E$  with  $\rho_{\text{me}}(E) \neq 0$  as localized if  $\rho_{\text{ty}}(E) = 0$  and as extended if  $\rho_{\text{ty}}(E) \neq 0$ .

In order to discuss possible localization phenomena let us investigate the behavior of the mean DOS for the quantum percolation models (19.42). As long as  $\epsilon_A$  and  $\epsilon_B$  do not differ too much there exists an asymmetric (if  $p \neq 0.5$ ) but still connected electronic band [22]. At about  $\Delta \simeq 4tD$  this band separates into two sub-bands centered at  $\epsilon_A$  and  $\epsilon_B$ , respectively. The most prominent feature in the split-band regime is the series of spikes at discrete energies within the band. As an obvious guess, we might attribute these spikes to eigenstates on islands of  $A$  or  $B$  sites being isolated from the main cluster [23, 24]. It turns out, however, that some of the spikes persist, even if we neglect all finite clusters and restrict the calculation to the spanning cluster of  $A$  sites,  $A_\infty$ . This is illustrated in the upper panels of Fig. 19.2, where we compare the DOS of the model (19.42) (at  $\Delta \rightarrow \infty$ ) to that of the spanning cluster only Hamiltonian. Increasing the concentration of accessible sites the mean DOS of the spanning cluster is evocative of the DOS of the simple cubic lattice, but even at large values of  $p$  a sharp peak structure remains at  $E = 0$  (cf. Fig. 19.2, lower panels). Note that the most dominant peaks at  $E/t = 0, \pm 1, \pm\sqrt{2}, (\pm 1 \pm \sqrt{5})/2, \dots$  correspond to eigenvalues of the tight-binding model on small clusters with different geometries. We can thus argue that the wavefunctions, which belong to these special energies, are localized on some dead ends of the spanning cluster. The assumption that the distinct peaks correspond to localized wavefunctions is corroborated by the fact that the typical DOS vanishes or, at least, shows

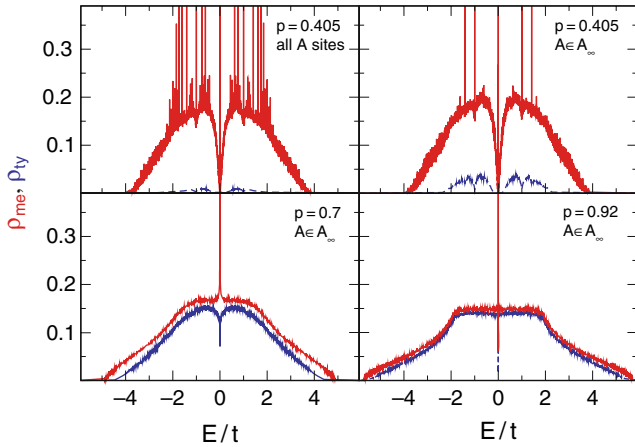


**Fig. 19.2.** Mean (*upper curves*) and typical (*lower curves*) DOS for the quantum percolation model in the limit  $\Delta \rightarrow \infty$ . While in the upper left panel all  $A$ -sites are taken into account, the other three panels show data for the restricted model on the spanning cluster  $A_\infty$  only (note that  $\rho_{ty}$  is smaller in the former case because there are more sites with vanishing amplitude of the wavefunction). System sizes were adapted to ensure that  $A_\infty$  always contains the same number of sites, i.e.,  $57^3$  for  $p = 0.405$ ,  $46^3$  for  $p = 0.70$ , and  $42^3$  for  $p = 0.92$ . In order to obtain these high-resolution data we used  $N = 32768$  Chebyshev moments and  $K_s \times K_r = 32 \times 32$

a dip at these energies. Occurring also for finite  $\Delta$ , this effect becomes more pronounced as  $\Delta \rightarrow \infty$  and in the vicinity of the classical percolation threshold  $p_c$ . For a more detailed discussion see [25].

### 19.2.2 Correlation Functions at Finite Temperature

Densities of states provide only the most basic information about a given quantum system, and much more details can usually be learned from the study of correlation functions.

Given the eigenstates  $|k\rangle$  of an interacting quantum system the thermodynamic expectation value of an operator  $A$  reads

$$\langle A \rangle = \frac{1}{ZD} \text{Tr}(Ae^{-\beta H}) = \frac{1}{ZD} \sum_{k=0}^{D-1} \langle k|A|k \rangle e^{-\beta E_k}, \quad (19.45)$$

where  $H$  is the Hamiltonian of the system,  $E_k$  the energy of the eigenstate  $|k\rangle$ , and  $Z = \text{Tr}(\exp(-\beta H))/D = D^{-1} \sum_{k=0}^{D-1} \exp(-\beta E_k)$  the partition function. Using the function  $a(E) = D^{-1} \sum_{k=0}^{D-1} \langle k|A|k \rangle \delta(E - E_k)$  and the (canonical) density of states  $\rho(E)$ , we can express the thermal expectation value in terms of integrals over the Boltzmann weight,

$$\langle A \rangle = \frac{1}{Z} \int_{-\infty}^{\infty} a(E) e^{-\beta E} dE, \quad Z = \int_{-\infty}^{\infty} \rho(E) e^{-\beta E} dE. \quad (19.46)$$

Of course, similar relations hold also for non-interacting fermion systems, where the Boltzmann weight  $\exp(-\beta E)$  has to be replaced by the Fermi function  $f(E) = 1/(1 + \exp(\beta(E - \mu)))$  and the single-electron wave functions play the role of  $|k\rangle$ .

Again, the particular form of  $a(E)$  suggests an expansion in Chebyshev polynomials, and after rescaling we find

$$\mu_n = \int_{-1}^1 \tilde{a}(E) T_n(E) dE = \frac{1}{D} \sum_{k=0}^{D-1} \langle k|A|k\rangle T_n(\tilde{E}_k) = \frac{1}{D} \text{Tr} \left( AT_n(\tilde{H}) \right), \quad (19.47)$$

which can be evaluated employing the stochastic approach, outlined in Sect. 19.1.

For interacting systems at low temperature the expression in (19.46) is a bit problematic, since the Boltzmann factor puts most of the weight on the lower end of the spectrum and heavily amplifies small numerical errors in  $\rho(E)$  and  $a(E)$ . We can avoid these problems by calculating the ground state and some of the lowest excitations exactly, using standard iterative diagonalization methods like Lanczos or Jacobi-Davidson (see Sect. 18.2). Then we split the expectation value of  $A$  and the partition function  $Z$  into contributions from the exactly known states and contributions from the rest of the spectrum,

$$\begin{aligned} \langle A \rangle &= \frac{1}{ZD} \sum_{k=0}^{C-1} \langle k|A|k\rangle e^{-\beta E_k} + \frac{1}{Z} \int_{-\infty}^{\infty} a_s(E) e^{-\beta E} dE, \\ Z &= \frac{1}{D} \sum_{k=0}^{C-1} e^{-\beta E_k} + \int_{-\infty}^{\infty} \rho_s(E) e^{-\beta E} dE. \end{aligned} \quad (19.48)$$

Here  $a_s(E) = D^{-1} \sum_{k=C}^{D-1} \langle k|A|k\rangle \delta(E - E_k)$  and  $\rho_s(E) = D^{-1} \sum_{k=C}^{D-1} \delta(E - E_k)$  describe the rest of the spectrum and can be expanded in Chebyshev polynomials easily. Based on the known states we can introduce the projection operator  $P = 1 - \sum_{k=0}^{C-1} |k\rangle\langle k|$  and find for the expansion coefficients of  $\tilde{a}_s(E)$

$$\mu_n = \frac{1}{D} \text{Tr}(PAT_n(\tilde{H})) \approx \frac{1}{RD} \sum_{r=0}^{R-1} \langle r|PAT_n(\tilde{H})P|r\rangle, \quad (19.49)$$

and similarly for those of  $\tilde{\rho}_s(E)$ :

$$\mu_n = \frac{1}{D} \text{Tr}(PT_n(\tilde{H})) \approx \frac{1}{RD} \sum_{r=0}^{R-1} \langle r|PT_n(\tilde{H})P|r\rangle. \quad (19.50)$$

Note, that in addition to the two vectors for the Chebyshev recursion we now need memory also for the eigenstates  $|k\rangle$ . Otherwise the resource consumption is the same as in the standard scheme.

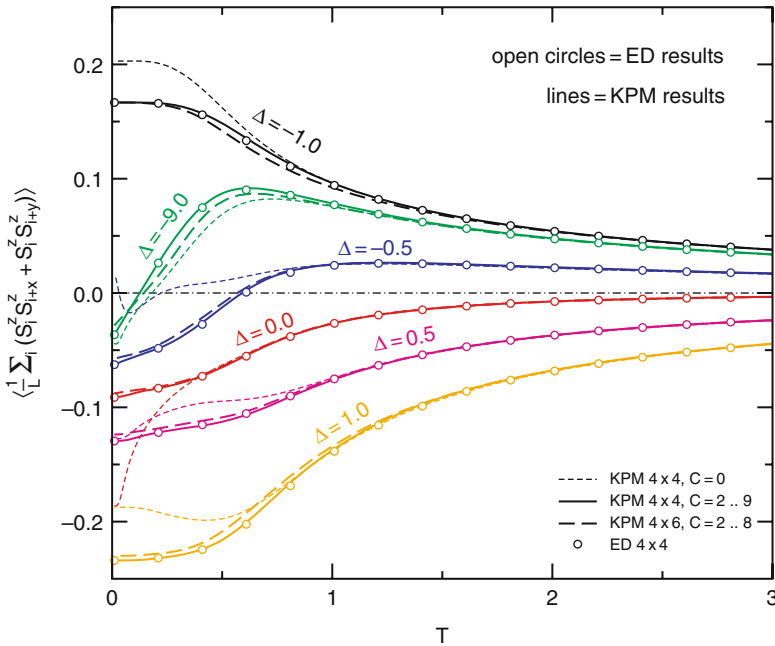


**Fig. 19.3.** Nearest-neighbor  $S^z$ - $S^z$  correlations of the XXZ model on a square lattice. Lines represent the KPM results with separation of low-lying eigenstates (*bold solid* and *bold dashed*) and without (*thin dashed*), open symbols denote exact results from a complete diagonalization of a  $4 \times 4$  system

We illustrate the accuracy of this approach in Fig. 19.3 considering the nearest-neighbor  $S^z$ - $S^z$  correlations of the square-lattice spin-1/2 XXZ model as an example,

$$H = \sum_{i,\delta} (S_i^x S_{i+\delta}^x + S_i^y S_{i+\delta}^y + \Delta S_i^z S_{i+\delta}^z). \quad (19.51)$$

As a function of temperature and for an anisotropy  $-1 < \Delta < 0$  this model shows a quantum to classical crossover in the sense that the correlations are anti-ferromagnetic at low temperature (quantum effect) and ferromagnetic at high temperature (as expected for the classical model) [26, 27, 28]. Comparing the KPM results with the exact correlations of a  $4 \times 4$  system, which were obtained from a complete diagonalization of the Hamiltonian, the improvement due to the separation of only a few low-lying eigenstates is obvious. Whereas for  $C = 0$  the data is more or less random below  $T \approx 1$ , the agreement with the exact data is perfect, if the ground state and one or two excitations are considered separately. The numerical effort required for these calculations differs largely between complete diagonalization and the KPM method. For the former, 18 or 20 sites are practically the limit, whereas the latter can easily handle 30 sites or more.

Note that for non-interacting systems the above separation of the spectrum is not required, since for  $T \rightarrow 0$  the Fermi function converges to a simple step function without causing any numerical problems.

### 19.2.3 Spectral Functions and Dynamical Response

#### 19.2.3.1 General Considerations

Having discussed simple expectation values and static correlations, the calculation of time dependent quantities is the natural next step in the study of complex quantum models. This is motivated also by many experimental setups, which probe the response of a physical system to time dependent external perturbations. Examples are inelastic scattering experiments or measurements of transport coefficients. In the framework of linear response theory and the Kubo formalism the system's response is expressed in terms of dynamical correlation functions, which can also be calculated efficiently with Chebyshev expansion and KPM.

Given two operators  $A$  and  $B$  a general dynamical correlation function can be defined through

$$\langle A; B \rangle_{\omega}^{\pm} = \lim_{\epsilon \rightarrow 0} \langle 0 | A \frac{1}{\omega + i\epsilon \mp H} B | 0 \rangle = \lim_{\epsilon \rightarrow 0} \sum_{k=0}^{D-1} \frac{\langle 0 | A | k \rangle \langle k | B | 0 \rangle}{\omega + i\epsilon \mp E_k}, \quad (19.52)$$

where  $E_k$  is the energy of the many-particle eigenstate  $|k\rangle$  of the Hamiltonian  $H$ ,  $|0\rangle$  its ground state, and  $\epsilon > 0$ .

If we assume that the product  $\langle 0 | A | k \rangle \langle k | B | 0 \rangle$  is real the imaginary part

$$\text{Im} \langle A; B \rangle_{\omega}^{\pm} = -\pi \sum_{k=0}^{D-1} \langle 0 | A | k \rangle \langle k | B | 0 \rangle \delta(\omega \mp E_k) \quad (19.53)$$

has a similar structure as, e.g., the local density of states in (19.43), and in fact, with  $\rho_i(E)$  we already calculated a dynamical correlation function. Rescaling the Hamiltonian  $H \rightarrow \tilde{H}$  and all energies  $\omega \rightarrow \tilde{\omega}$  we can proceed as usual and expand  $\text{Im} \langle A; B \rangle_{\tilde{\omega}}^{\pm}$  in Chebyshev polynomials,

$$\text{Im} \langle A; B \rangle_{\tilde{\omega}}^{\pm} = -\frac{1}{\sqrt{1 - \tilde{\omega}^2}} \left( \mu_0 + 2 \sum_{n=1}^{\infty} \mu_n T_n(\tilde{\omega}) \right). \quad (19.54)$$

Again, the moments are obtained from expectation values

$$\mu_n = \frac{1}{\pi} \int_{-1}^1 \text{Im} \langle A; B \rangle_{\tilde{\omega}}^{\pm} T_n(\tilde{\omega}) d\tilde{\omega} = \langle 0 | A T_n(\mp \tilde{H}) B | 0 \rangle. \quad (19.55)$$

In many cases, especially for the spectral functions and optical conductivities studied below, only the imaginary part of  $\langle A; B \rangle_{\omega}^{\pm}$  is of interest, and the above setup

is all we need. Sometimes however – e.g., within the cluster perturbation theory discussed in Sect. 19.3 – also the real part of a general correlation function  $\langle A; B \rangle_{\tilde{\omega}}^{\pm}$  is required. Fortunately it can be calculated with almost no additional effort: The analytical properties of  $\langle A; B \rangle_{\tilde{\omega}}^{\pm}$  arising from causality imply that its real part is fully determined by the imaginary part. Indeed, using the Hilbert transforms of the Chebyshev polynomials,

$$\begin{aligned} \mathcal{P} \int_{-1}^1 \frac{T_n(y) dy}{(y-x)\sqrt{1-y^2}} &= \pi U_{n-1}(x), \\ \mathcal{P} \int_{-1}^1 \frac{\sqrt{1-y^2} U_{n-1}(y) dy}{(y-x)} &= -\pi T_n(x), \end{aligned} \quad (19.56)$$

we obtain

$$\begin{aligned} \text{Re} \langle A; B \rangle_{\tilde{\omega}}^{\pm} &= \sum_{k=0}^{D-1} \langle 0|A|k \rangle \langle k|B|0 \rangle \mathcal{P} \left( \frac{1}{\tilde{\omega} \mp \tilde{E}_k} \right) \\ &= -\frac{1}{\pi} \mathcal{P} \int_{-1}^1 \frac{\text{Im} \langle A; B \rangle_{\tilde{\omega}'}^{\pm}}{\tilde{\omega} - \tilde{\omega}'} d\omega' = -2 \sum_{n=1}^{\infty} \mu_n U_{n-1}(\tilde{\omega}). \end{aligned} \quad (19.57)$$

The full correlation function

$$\begin{aligned} \langle A; B \rangle_{\tilde{\omega}}^{\pm} &= \frac{-i\mu_0}{\sqrt{1-\tilde{\omega}^2}} - 2 \sum_{n=1}^{\infty} \mu_n \left( U_{n-1}(\tilde{\omega}) + \frac{i T_n(\tilde{\omega})}{\sqrt{1-\tilde{\omega}^2}} \right) \\ &= \frac{-i}{\sqrt{1-\tilde{\omega}^2}} \left( \mu_0 + 2 \sum_{n=1}^{\infty} \mu_n e^{-in \arccos \tilde{\omega}} \right) \end{aligned} \quad (19.58)$$

can thus be reconstructed from the same moments  $\mu_n$  that we derived for its imaginary part (19.55). In contrast to the real quantities we considered so far, the reconstruction merely requires complex Fourier transform (see (19.39)). If only the imaginary or real part of  $\langle A; B \rangle_{\tilde{\omega}}^{\pm}$  is needed, a cosine or sine transform, respectively, is sufficient.

Note that the calculation of dynamical correlation functions for non-interacting electron systems is not possible with the scheme discussed in this section, not even at zero temperature. At finite band filling (finite chemical potential) the ground state consists of a sum over occupied single-electron states, and dynamical correlation functions thus involve a double summation over matrix elements between all single-particle eigenstates, weighted by the Fermi function. See the section on the optical conductivity for a discussion of this case, which covers also the calculation of dynamical correlation functions at finite temperature.

### 19.2.3.2 One-Particle Spectral Function

An important example of a dynamical correlation function is the (retarded) Green function in momentum space,

$$G_\sigma(\mathbf{k}, \omega) = \langle c_{\mathbf{k},\sigma}; c_{\mathbf{k},\sigma}^\dagger \rangle_\omega^+ + \langle c_{\mathbf{k},\sigma}^\dagger; c_{\mathbf{k},\sigma} \rangle_\omega^-, \quad (19.59)$$

and the associated spectral function

$$A_\sigma(\mathbf{k}, \omega) = -\frac{1}{\pi} \text{Im} G_\sigma(\mathbf{k}, \omega) = A_\sigma^+(\mathbf{k}, \omega) + A_\sigma^-(\mathbf{k}, \omega), \quad (19.60)$$

which characterizes the electron absorption or emission of an interacting system. For instance,  $A^-$  can be measured experimentally in angle resolved photo-emission spectroscopy (ARPES).

Exemplarily let us consider the one-dimensional Holstein model

$$H = -t \sum_i (c_i^\dagger c_{i+1} + \text{H.c.}) - g\omega_0 \sum_{i,\sigma} (b_i^\dagger + b_i) n_{i,\sigma} + \omega_0 \sum_i b_i^\dagger b_i, \quad (19.61)$$

which is one of the basic models for the study of electron-lattice interaction in electronically low-dimensional solids. In (19.61), the electrons are approximated by spinless fermions  $c_i^{(\dagger)}$ , the density of which couples to the local lattice distortion described by dispersionless phonons  $b_i^{(\dagger)}$ . At half-filling, i.e., 0.5 fermions per site, the model allows for the study of quantum effects at the transition from a (Luttinger liquid) metal to a (Peierls) insulator, marked by the opening of a gap at the Fermi wave vector and the development of charge-density-wave (CDW) long-range order and a matching lattice distortion [29, 30, 31]. The Peierls insulator can be classified as traditional band insulator and polaronic superlattice in the strong electron-phonon coupling adiabatic ( $\omega_0/t \ll 1$ ) and anti-adiabatic ( $\omega_0/t \gg 1$ ) regimes, respectively.

Figure 19.4 shows KPM data for the spectral function of the half-filled Holstein model and assesses its quality by comparing with results from Dynamical Density Matrix Renormalization Group (DDMRG) [32] calculations. In the spinless case, the photo-emission ( $A^-$ ) and inverse photo-emission ( $A^+$ ) parts read

$$\begin{aligned} A^-(k, \omega) &= \sum_l |\langle l, N_e - 1 | c_k | 0, N_e \rangle|^2 \delta[\omega + (E_{l, N_e - 1} - E_{0, N_e})], \\ A^+(k, \omega) &= \sum_l |\langle l, N_e + 1 | c_k^\dagger | 0, N_e \rangle|^2 \delta[\omega - (E_{l, N_e + 1} - E_{0, N_e})], \end{aligned} \quad (19.62)$$

where  $|l, N_e\rangle$  denotes the  $l$ th eigenstate with  $N_e$  electrons and energy  $E_{l, N_e}$ . For the parameters of Fig. 19.4 the system is in an insulating phase with a finite charge excitation gap at the Fermi momentum  $k = \pm\pi/2$ . Below and above the gap the spectrum is characterized by broad multi-phonon absorption, reflecting the Poisson-like phonon distribution in the ground state. Compared to DDMRG, KPM offers the better resolution and unfolds all the discrete phonon sidebands. Concerning numerical performance DDMRG has the advantage of a small optimized Hilbert space

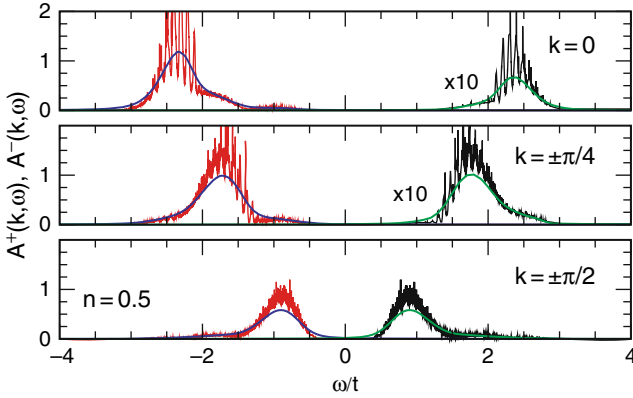


**Fig. 19.4.** Single-particle spectral functions  $A(k, \omega)$  (for electron removal,  $\omega < 0$ , and electron injection,  $\omega > 0$ ) of the spinless Holstein model at half-filling on an eight-site lattice with periodic boundary conditions. The system is in the Peierls/CDW insulating phase ( $\omega_0/t = 0.1$  and  $g = 4$ ). The rapidly oscillating thin lines are the KPM results ( $M = 32$ ) while the smooth thick line are the DDMRG data ( $M = 16$ ) obtained with the pseudo-site method for the same lattice size

[33, 34], which can be handled with standard workstations. However, the basis optimization is rather time consuming and, in addition, each frequency value  $\omega$  requires a new simulation. The KPM calculations, on the other hand, involved matrix dimensions between  $10^8$  and  $10^{10}$ , and we therefore used high-performance computers such as Hitachi SR8000-F1 or IBM p690 for the moment calculation. For the reconstruction of the spectra, of course, a desktop computer is sufficient.

### 19.2.3.3 Optical Conductivity

The next example of a dynamical correlation function is the optical conductivity. Here the imaginary and real parts of our general correlation functions  $\langle A; B \rangle_\omega$  change their roles due to an additional frequency integration. The so-called regular contribution to the real part of the optical conductivity is thus given by,

$$\sigma^{\text{reg}}(\omega) = \frac{1}{\omega} \sum_{E_k > E_0} |\langle k|J|0\rangle|^2 \delta(\omega - (E_k - E_0)), \quad (19.63)$$

with the current operator  $J = -igt \sum_{i,\sigma} (c_{i,\sigma}^\dagger c_{i+1,\sigma} - \text{H.c.})$ . The latter follows from the continuity equation  $\dot{n}_{i\sigma} = i[H, n_{i\sigma}] = j_{i-1,\sigma} - j_{i\sigma}$ , where  $j_{i\sigma}$  is the local particle current. After rescaling the energy and shifting the frequency,  $\omega = \tilde{\omega} + \tilde{E}_0$ , the sum can be expanded as described earlier, now with  $J|0\rangle$  as the initial state for the Chebyshev recursion. Back-scaling and dividing by  $\omega$  then yields the final result.

The finite-temperature extension of (19.63) is given by

$$\sigma^{\text{reg}}(\omega) = \sum_{k,q} \frac{|\langle k|J|q\rangle|^2 (e^{-\beta E_k} - e^{-\beta E_q})}{Z D \omega} \delta(\omega - \omega_{qk}), \quad (19.64)$$

with  $\omega_{qk} = E_q - E_k$ . Compared to (19.63) a straight-forward expansion of the finite temperature conductivity is spoiled by the presence of the Boltzmann weighting factors. A solution comes from the current matrix element density

$$j(x, y) = \frac{1}{D} \sum_{k,q} |\langle k|J|q\rangle|^2 \delta(x - E_k) \delta(y - E_q) . \quad (19.65)$$

Being a function of two variables,  $j(x, y)$  can be expanded with two-dimensional KPM,

$$\tilde{j}(x, y) = \sum_{n,m=0}^{N-1} \frac{\mu_{nm} h_{nm} g_n g_m T_n(x) T_m(y)}{\pi^2 \sqrt{(1-x^2)(1-y^2)}} , \quad (19.66)$$

where  $\tilde{j}(x, y)$  refers to the rescaled  $j(x, y)$ ,  $g_n$  are the usual kernel damping factors, and  $h_{nm}$  account for the correct normalization. The moments  $\mu_{nm}$  are obtained from

$$\mu_{nm} = \int_{-1}^1 \int_{-1}^1 \tilde{j}(x, y) T_n(x) T_m(y) dx dy = \frac{1}{D} \text{Tr} (T_n(\tilde{H}) J T_m(\tilde{H}) J) , \quad (19.67)$$

and again the trace can be replaced by an average over a relatively small number  $R$  of random vectors  $|r\rangle$ . The numerical effort for an expansion of order  $n, m < N$  ranges between  $2RDN$  and  $RDN^2$  operations, depending on whether memory is available for up to  $N$  vectors of the Hilbert space dimension  $D$  or not. Given the operator density  $j(x, y)$  we find the optical conductivity by integrating over Boltzmann factors,

$$\begin{aligned} \sigma^{\text{reg}}(\omega) &= \frac{1}{Z\omega} \int_{-\infty}^{\infty} j(y + \omega, y) (e^{-\beta y} - e^{-\beta(y+\omega)}) dy \\ &= \sum_{k,q} \frac{|\langle k|J|q\rangle|^2 (e^{-\beta E_k} - e^{-\beta E_q})}{ZD\omega} \delta(\omega - \omega_{qk}) , \end{aligned} \quad (19.68)$$

and, as above, we get the partition function  $Z$  from an integral over the density of states  $\rho(E)$ . The latter can be expanded in parallel to  $j(x, y)$ . Note that the calculation of the conductivity at different temperatures is based on the same operator density  $j(x, y)$ , i.e., it needs to be expanded only once for all temperatures.

As a physical example, we consider the conductivity for the Anderson model of non-interacting fermions moving in a random potential [18],

$$H = -t \sum_{\langle ij \rangle} c_i^\dagger c_j + \sum_i \epsilon_i c_i^\dagger c_i . \quad (19.69)$$

Here hopping occurs along nearest neighbor bonds  $\langle ij \rangle$  on a simple cubic lattice and the local potential  $\epsilon_i$  is chosen randomly with uniform distribution in the interval  $[-\gamma/2, \gamma/2]$ . With increasing strength of disorder,  $\gamma$ , the single-particle eigenstates of the model tend to become localized in the vicinity of a particular lattice

site, which excludes these states from contributing to electronic transport. Disorder can therefore drive a transition from metallic behavior with delocalized fermions to insulating behavior with localized fermions [35, 36, 37].

Since the Anderson model describes non-interacting fermions, the eigenstates  $|k\rangle$  occurring in  $\sigma(\omega)$  now denote single-particle wave functions and the Boltzmann weight has to be replaced by the Fermi function,

$$\sigma^{\text{reg}}(\omega) = \sum_{k,q} \frac{|\langle k|J|q\rangle|^2 (f(E_k) - f(E_q))}{\omega} \delta(\omega - \omega_{qk}) . \quad (19.70)$$

Clearly, from a computational point of view this expression is of the same complexity for both, zero and finite temperature, i.e. we need the more advanced 2D KPM approach [38].

Figure 19.5 shows the optical conductivity of the Anderson model at  $\gamma/t = 12$  for different inverse temperatures  $\beta = 1/T$ . The chemical potential is chosen as  $\mu = 0$ , i.e., the system is still in the metallic phase. However, the conductivity shows a pronounced dip near  $\omega = 0$  with the functional form  $\sigma(\omega) \sim \sigma_0 + |\omega|^\alpha$ . For stronger disorder  $\gamma$  or a different chemical potential  $\mu$ , the system will become insulating and the dc-conductivity  $\sigma_0$  will vanish. The role of temperature, in this example, is limited to suppressing  $\sigma(\omega)$ , mainly through the  $(f(E_k) - f(E_q))$  term in (19.70). The model (19.69) does not describe thermally activated hopping, since there are no phonons included.

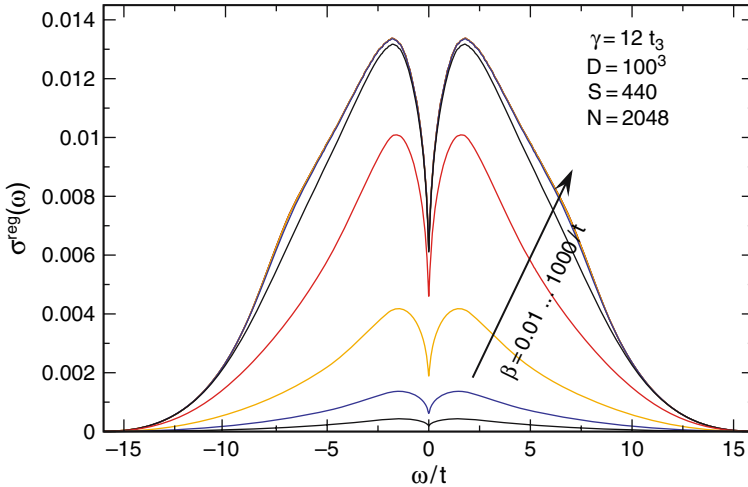


**Fig. 19.5.** Optical conductivity of the 3D Anderson model with  $\gamma = 12$ . Note that all curves are derived from the same matrix element density  $j(x, y)$ , which was calculated for a  $100^3$  site cluster with expansion order  $N = 2048$  and averaged over  $K_\tau = 440$  samples

### 19.2.4 Time Evolution of Quantum Systems

Dynamical correlation functions are an important aspect in the description of interacting quantum systems and, in many cases, are directly related to experimental results, in particular spectroscopy data. On the other hand, new experimental setups and techniques led to an increased interest in the real time dynamics of quantum systems. Chebyshev expansion is applicable also in this situation.

Starting from the time dependent Schrödinger equation,

$$i\partial_t|\psi\rangle = H|\psi\rangle, \quad (19.71)$$

the approach is surprisingly simple: Assuming that at time  $t = 0$  the system is in the state  $|\psi_0\rangle$ , its state at a later time is

$$|\psi_t\rangle = e^{-iHt}|\psi_0\rangle, \quad (19.72)$$

and the problem translates into calculating the time evolution operator  $U(t) = \exp(-iHt)$  for a given Hamiltonian  $H$  and time  $t$ . Using the rescaling introduced in (19.7), we can expand  $U(t)$  in a series of Chebyshev polynomials [39, 40, 41],

$$U(t) = e^{-i(a\tilde{H}+b)t} = e^{-ibt} \left( c_0 + 2 \sum_{k=1}^N c_k T_k(\tilde{H}) \right), \quad (19.73)$$

where the expansion coefficients  $c_k$  are given by

$$c_k = \int_{-1}^1 \frac{T_k(x)e^{-iaxt}}{\pi\sqrt{1-x^2}} dx = (-i)^k J_k(at), \quad (19.74)$$

and  $J_k(at)$  denotes the Bessel function of order  $k$ . The Chebyshev polynomials of the Hamiltonian,  $T_k(\tilde{H})$ , are calculated with the recursion we introduced earlier, see (19.3). Thus, the wave function at a later time is obtained simply through a set of MVMs with the Hamiltonian.

Asymptotically the Bessel function behaves as

$$J_k(z) \sim \frac{1}{k!} \left(\frac{z}{2}\right)^k \sim \frac{1}{\sqrt{2\pi k}} \left(\frac{ez}{2k}\right)^k \quad (19.75)$$

for  $k \rightarrow \infty$ , hence for  $k \gg at$  the expansion coefficients  $c_k$  decay superexponentially and the series can be truncated with negligible error. With an expansion order of  $N \gtrsim 1.5at$  we are usually on the safe side. Moreover, we can check the quality of our approximation by comparing the norms of  $|\psi_t\rangle$  and  $|\psi_0\rangle$ . For sparse matrices the whole time evolution scheme is therefore linear in both, the matrix dimension and the time.

The Chebyshev expansion method converges much faster than other time integration methods, in particular, it is faster than the popular Crank-Nicolson method

[42]. Within this approach the time interval  $t$  is divided into small steps  $\Delta t = t/N$ , and the wave function is propagated in a mixed explicit/implicit manner,

$$(1 + \frac{1}{2}iH\Delta t)|\psi_{n+1}\rangle = (1 - \frac{1}{2}iH\Delta t)|\psi_n\rangle. \quad (19.76)$$

Thus, each step requires both a sparse MVM and the solution of a sparse linear system. Obviously, this is more complicated than the Chebyshev recursion, which requires only MVMs. In the Crank-Nicolson method the time evolution operator is approximated as

$$U(t) = \left( \frac{1 - iHt/(2N)}{1 + iHt/(2N)} \right)^N. \quad (19.77)$$

In Fig. 19.6 we compare this approximation with the Chebyshev approximation by replacing  $H$  with the real variable  $x$  (this is equivalent to working with a diagonal matrix  $H$ ). In both cases we consider time  $t = 10$  and expansion order  $N = 15$ . Whereas the Chebyshev result agrees perfectly with the exact result  $\exp(ixt)$ , the Crank-Nicolson approximation needs much higher  $N$  to achieve the same accuracy ( $N \approx 90$ ).

Having explained the time evolution algorithm, let us now consider a specific example: the formation of a polaron on an one-dimensional lattice. The Hamiltonian for this problem was introduced at the beginning of this chapter, see (18.3). The polaron problem corresponds to the case of a single electron interacting with finite frequency lattice vibrations, i.e., we can omit the spin indices and the Hubbard term does not contribute. Bonča, Trugman and co-workers [43, 44] introduced a highly efficient variational basis for the polaron problem, which can be used to study its ground-state properties and lowest excitations on an infinite lattice, as well as the

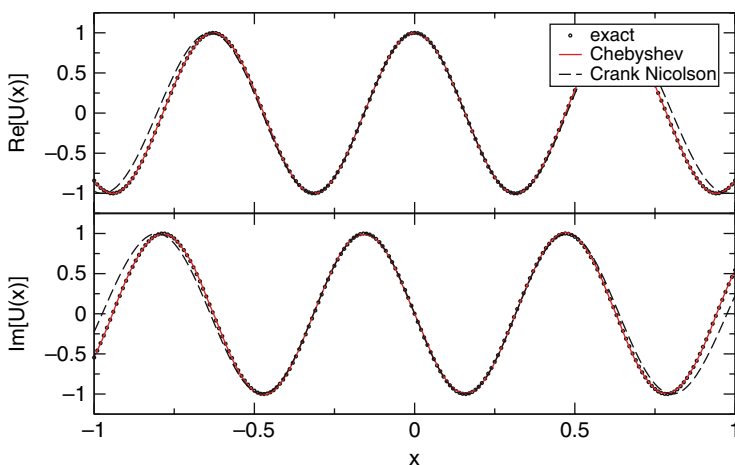


**Fig. 19.6.** Comparison of the Chebyshev and the Crank-Nicolson approximation of the function  $U(t) = \exp(ixt)$  with  $t = 10$  and expansion order  $N = 15$

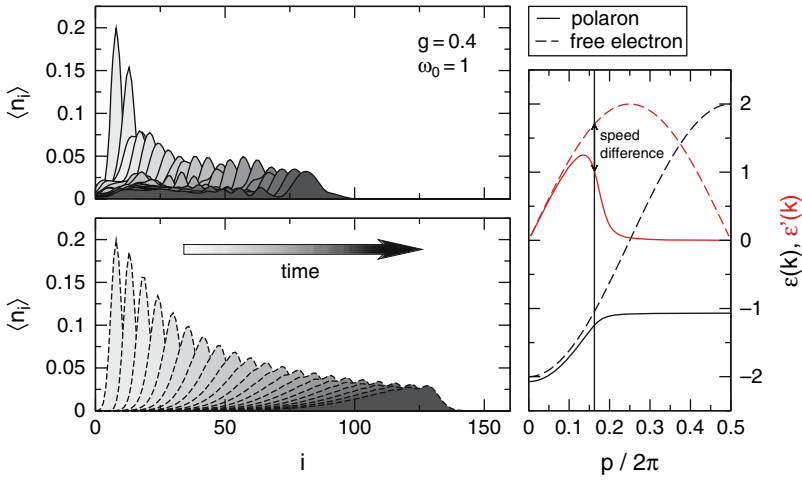


**Fig. 19.7.** Formation of a polaron for electron-lattice coupling  $g = 0.4$  and phonon frequency  $\omega_0 = 1$  (**upper panel**), compared to the motion of a non-interacting wave packet (**lower panel**). The right panel shows the underlying dispersions (*lower curves*) and velocities (*upper curves*)

quantum dynamics of such a system (for a recent review see also [45]). In Fig. 19.7 we show the time evolution of a single-electron wave packet

$$|\psi_0\rangle = \sum_j e^{ipj - (j-j_0)^2 / (2\sigma^2)} c_j^\dagger |0\rangle, \tag{19.78}$$

where in the upper and lower panels the electron-phonon coupling  $g$  is finite or zero, respectively. For finite  $g$ , within the first few time steps a polaron is formed, which then travels at lower speed, compared to the non-interacting wave packet. The speed difference is given by the difference of the derivatives  $\varepsilon'(k)$  of the underlying dispersions  $\varepsilon(k)$  at the mean momentum  $p$ , see right hand panel. The Chebyshev expansion method allows for a fast and reliable simulation of this interesting problem.

## 19.3 KPM in Relation to other Numerical Approaches

### 19.3.1 KPM and CPT

The spectrum of a finite system of  $L$  sites, which we obtain through KPM, differs in many respects from that of an infinite system,  $L \rightarrow \infty$ , especially since for a finite system the lattice momenta  $K = \pi m/L$  and the energy levels are discrete. While we cannot easily increase  $L$  without reaching computationally inaccessible Hilbert space dimensions, we can try to extrapolate from a finite to the infinite system.

With the Cluster Perturbation Theory (CPT) [46, 47, 48] a straightforward way to perform this task approximatively has recently been devised. In this scheme one

first calculates the Green function  $G_{ij}^c(\omega)$  for all sites  $i, j = 1, \dots, L$  of a  $L$ -size cluster with open boundary conditions, and then recovers the infinite lattice by pasting identical copies of this cluster at their edges. The glue is the hopping  $V$  between these clusters, where  $V_{mn} = t$  for  $|m - n| = 1$  and  $m, n \equiv 0, 1 \pmod{L}$ , which is dealt with in first order perturbation theory. Then the Green function  $G_{ij}(\omega)$  of the infinite lattice is given through a Dyson equation

$$G_{ij}(\omega) = G_{ij}^c(\omega) + \sum_{mn} G_{ik}^c(\omega) V_{mn} G_{nj}(\omega), \quad (19.79)$$

where indices of  $G^c(\omega)$  are counted modulo  $L$ . Obviously this order of perturbation in  $V$  is exact for the non-interacting system. The Dyson equation is solved by Fourier transformation over momenta  $K = kL$  corresponding to translations by  $L$  sites

$$G_{ij}(K, \omega) = \left[ \frac{G^c(\omega)}{1 - V(K)G^c(\omega)} \right]_{ij}. \quad (19.80)$$

from which one finally obtains

$$G(k, \omega) = \frac{1}{L} \sum_{i,j=1}^L G_{ij}^c(Lk, \omega) e^{-ik(i-j)}. \quad (19.81)$$

Hence, from the Green function  $G_{ij}^c(\omega)$  on a finite cluster we construct a Green function  $G(k, \omega)$  with continuous momenta  $k$ .

Two approximations are made, one by using first order perturbation theory in  $V = t$ , the second on assuming translational symmetry in  $G_{ij}(\omega)$  which is satisfied only approximately. In principle, the CPT spectral function  $G(k, \omega)$  does not contain any more information than the cluster Green function  $G_{ij}^c(\omega)$  already does. But extrapolating to the infinite system it gives a first hint at the scenario in the thermodynamic limit. Providing direct access to spectral functions, still without relying on possibly erroneous approximations, CPT occupies a niche between variational approaches like (D)DMRG [32, 49] and methods directly working in the thermodynamic limit like the variational ED method [43].

On applying the CPT crucial attention has to be paid to the kernel used in the reconstruction of  $G_{ij}^c(\omega)$ . As it turns out, the Jackson kernel is an inadequate choice here, since already for the non-interacting tight-binding model it introduces spurious structures into the spectra [1]. The failure can be attributed to the shape of the Jackson kernel: Being optimized for high resolution, a pole in the Green function will give a sharp peak with most of its weight concentrated at the center, and rapidly decaying tails. The reconstructed (cluster) Green function therefore does not satisfy the correct analytical properties required in the CPT step. To guarantee these properties, instead, we use the Lorentz kernel, which is constructed in order to mimic the effect of a finite imaginary part in the energy argument of a Green function.

Using  $G_{ij}^c(\omega) = G_{ji}^c(\omega)$  (no magnetic field), for a  $L$ -site chain  $L$  diagonal and  $L(L-1)/2$  off-diagonal elements of  $G_{ij}^c(\omega)$  have to be calculated. The latter can be reduced to Chebyshev iterations for the operators  $c_i^{(\dagger)} + c_j^{(\dagger)}$ . The numerical effort

can be further reduced by a factor  $1/L$ : If we keep the ground state  $|0\rangle$  of the system we can calculate the moments  $\mu_n^{ij} = \langle 0 | c_i T_n(\tilde{H}) c_j^\dagger | 0 \rangle$  for  $L$  elements  $i = 1, \dots, L$  of  $G_{ij}^c(\omega)$  in a single Chebyshev iteration. To achieve a similar reduction within the Lanczos recursion we had to explicitly construct the eigenstates to the Lanczos eigenvalues. Then the factor  $1/L$  is exceeded by at least  $ND$  additional operations for the construction of  $N$  eigenstates of a  $D$ -dimensional sparse matrix. Hence using KPM for the CPT cluster diagonalization the numerical effort can be reduced by a factor of  $1/L$  in comparison to the Lanczos recursion.

As an example we consider the 1D Hubbard model

$$H = -t \sum_{i,\sigma} (c_{i,\sigma}^\dagger c_{i+1,\sigma} + \text{H.c.}) + U \sum_i n_{i\uparrow} n_{i\downarrow}, \quad (19.82)$$

which is exactly solvable by Bethe ansatz [50] and was also extensively studied with DDMRG [51]. It thus provides the opportunity to assess the precision of the KPM-based CPT. The top left panel of Fig. 19.8 shows the one-particle spectral function at half-filling, calculated on the basis of  $L = 16$  site clusters and an expansion order of  $N = 2048$ . The matrix dimension is  $D \approx 1.7 \cdot 10^8$ . Remember that the cluster Green function is calculated for a chain with open boundary conditions. The reduced symmetry compared to periodic boundary conditions results in a larger dimension of the Hilbert space that has to be dealt with numerically.

In the top right panel the dots show the Bethe ansatz results for a  $L = 64$  site chain, and the lines denote the  $L \rightarrow \infty$  spinon and holon excitations each electron separates into (spin-charge separation). So far the Bethe ansatz does not allow for a direct calculation of the structure factor, the data thus represents only the position and density of the eigenstates, but is not weighted with the matrix elements of the operators  $c_{k\sigma}^{(\dagger)}$ . Although for an infinite system we would expect a continuous response, the CPT data shows some faint fine-structure. A comparison with the finite-size Bethe ansatz data suggests that these features are an artifact of the finite-cluster Greens function which the CPT spectral function is based on. The fine-structure is also evident in the lower panel of Fig. 19.8, where we compare with DDMRG data for a  $L = 128$  site system. Otherwise the CPT nicely reproduces all expected features, like the excitation gap, the two pronounced spinon and holon branches, and the broad continuum. Note also, that CPT is applicable to all spatial dimensions, whereas DDMRG works well only for 1D models.

### 19.3.2 Chebyshev Expansion and Maximum Entropy

Having demonstrated the wide applicability of KPM, let us now discuss some direct competitors of KPM, i.e., methods that share the broad application range and some of its general concepts.

The first of these approaches, the combination of Chebyshev expansion and Maximum Entropy Method (MEM), is basically an alternative procedure to transform moment data  $\mu_n$  into convergent approximations of the considered function

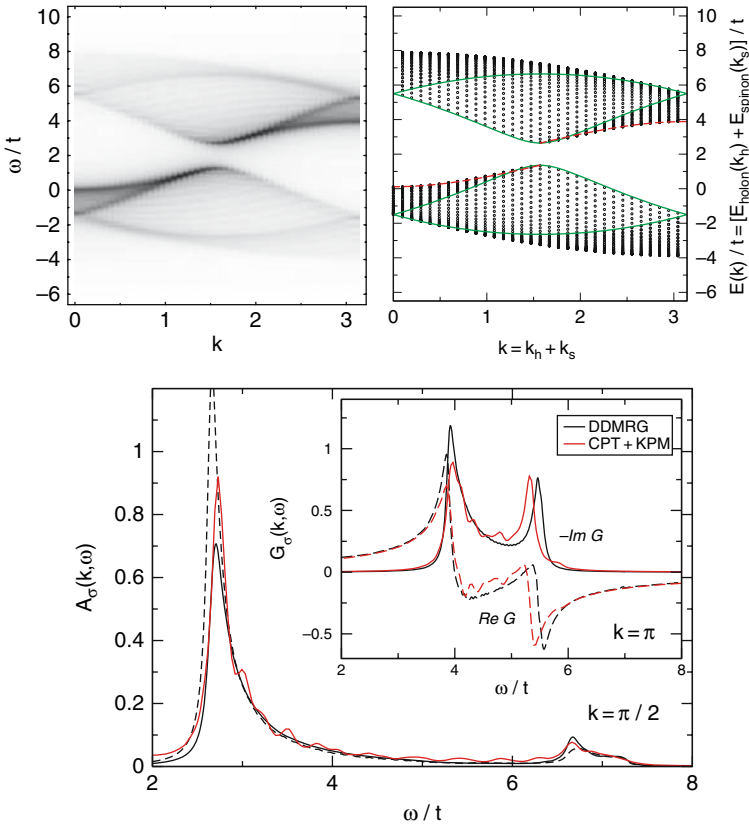


**Fig. 19.8.** Spectral function of the 1D Hubbard model for half-filling and  $U = 4t$ . **Top left:** CPT result with cluster size  $L = 16$  and expansion order  $N = 2048$ . For similar data based on Lanczos recursion see [47]. **Top right:** Within the exact Bethe ansatz solution each electron separates into the sum of independent spinon (red dashed) and holon (green) excitations. The dots mark the energies of a 64-site chain. **Bottom:** CPT data compared to selected DDMRG results for a system with  $L = 128$  sites, open boundary conditions and a broadening of  $\epsilon = 0.0625t$ . Note that in DDMRG the momenta are approximate

$f(x)$ . To achieve this, instead of (or in addition to) applying kernel polynomials, an entropy

$$S(f, f_0) = \int_{-1}^1 \left[ f(x) - f_0(x) - \log \left( \frac{f(x)}{f_0(x)} \right) \right] dx \quad (19.83)$$

is maximized under the constraint that the moments of the estimated  $f(x)$  agree with the given data. The function  $f_0(x)$  describes our initial knowledge about  $f(x)$ , and may in the worst case just be a constant. Being related to Maximum Entropy approaches to the classical moment problem [52, 53], for the case of Chebyshev moments different implementations of MEM have been suggested [9, 54, 55]. Since

for a given set of  $N$  moments  $\mu_n$  the approximation to the function  $f(x)$  is usually not restricted to a polynomial of degree  $N - 1$ , compared to the KPM with Jackson kernel the MEM usually yields estimates of higher resolution. However, this higher resolution results from adding a priori assumptions and not from a true information gain (see also Fig. 19.9). The resource consumption of the MEM is generally much higher than the  $N \log N$  behavior we found for KPM. In addition, the approach is non-linear in the moments and can occasionally become unstable for large  $N$ . Note also that as yet MEM have been derived only for positive quantities,  $f(x) > 0$ , such as densities of states or strictly positive correlation functions.

MEM, nevertheless, is a good alternative to KPM, if the calculation of the  $\mu_n$  is particularly time consuming. Based on only a moderate number of moments it yields very detailed approximations of  $f(x)$ , and we obtained very good results for some computationally demanding problems [56].

### 19.3.3 Lanczos Recursion

The Lanczos recursion technique [57] is certainly the most capable competitor of KPM. The use of the Lanczos algorithm [8, 58] for the characterization of spectral densities [59, 60] was first proposed at about the same time as the Chebyshev expansion approaches, and in principle Lanczos recursion is also a kind of modified moment expansion [61, 62]. Its generalization from spectral densities to zero-temperature dynamical correlation functions was first given in terms of continued fractions [63], and later also an approach based on the eigenstates of the tridiagonal matrix was introduced and termed Spectral Decoding Method [64]. This technique

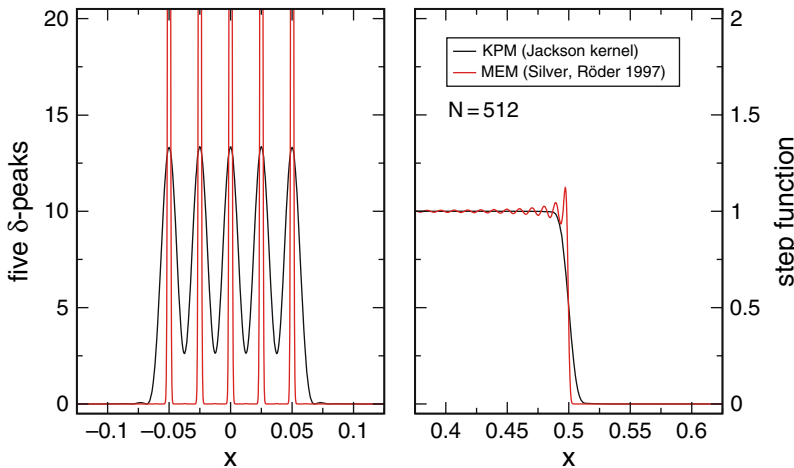


**Fig. 19.9.** Comparison of a KPM and a MEM approximation to a spectrum consisting of five isolated  $\delta$ -peaks, and to a step function. The expansion order is  $N = 512$ . Clearly, for the  $\delta$ -peaks MEM yields a higher resolution, but for the step function the Gibbs oscillations return (algorithm of [54])

was then generalized to finite temperature [65, 66], and, in addition, some variants of the approach for low temperature [67] and based on the micro-canonical ensemble [68] have been proposed recently.

To give an impression, in Table 19.1 we compare the setup for the calculation of a zero-temperature dynamical correlation function within the Chebyshev and the Lanczos approach. The most time consuming step for both methods is the recursive construction of a set of vectors  $|\phi_n\rangle$ , which in terms of scalar products yield the moments  $\mu_n$  of the Chebyshev series or the elements  $\alpha_n, \beta_n$  of the Lanczos tridiagonal matrix. In terms of the number of operations the Chebyshev recursion has a

**Table 19.1.** Comparison of Chebyshev expansion and Lanczos recursion for the calculation of a zero-temperature dynamical correlation function  $f(\omega) = \sum_n |\langle n|A|0\rangle|^2 \delta(\omega - \omega_n)$ . We assume  $N$  MVMs with a  $D$ -dimensional sparse matrix  $H$ , and a reconstruction of  $f(\omega)$  at  $M$  points  $\omega_i$

Chebyshev / KPM	Lanczos recursion
Initialization:	Initialization:
$\tilde{H} = (H - b)/a$ $ \phi_0\rangle = A 0\rangle, \quad  \phi_1\rangle = \tilde{H} \phi_0\rangle$ $\mu_0 = \langle \phi_0   \phi_0 \rangle, \quad \mu_1 = \langle \phi_1   \phi_0 \rangle$	$\beta_0 = \sqrt{\langle 0   A^\dagger A   0 \rangle}$ $ \phi_0\rangle = A 0\rangle/\beta_0, \quad  \phi_{-1}\rangle = 0$
$O(ND)$	$O(ND)$
Recursion for $2N$ moments $\mu_n$ :	Recursion for $N$ coefficients $\alpha_n, \beta_n$ :
$ \phi_{n+1}\rangle = 2\tilde{H} \phi_n\rangle -  \phi_{n-1}\rangle$ $\mu_{2n+2} = 2\langle \phi_{n+1}   \phi_{n+1} \rangle - \mu_0$ $\mu_{2n+1} = 2\langle \phi_{n+1}   \phi_n \rangle - \mu_1$	$ \phi'\rangle = H \phi_n\rangle - \beta_n \phi_{n-1}\rangle, \quad \alpha_n = \langle \phi_n   \phi' \rangle$ $ \phi''\rangle =  \phi'\rangle - \alpha_n \phi_n\rangle, \quad \beta_{n+1} = \sqrt{\langle \phi''   \phi'' \rangle}$ $ \phi_{n+1}\rangle =  \phi''\rangle/\beta_{n+1}$
→ very stable	→ tends to lose orthogonality
$O(M \log M)$	$O(NM)$
Reconstruction in three simple steps:	Reconstruction via continued fraction:
Apply kernel: $\tilde{\mu}_n = g_n \mu_n$ Fourier transform: $\tilde{\mu}_n \rightarrow \tilde{f}(\tilde{\omega}_i)$ Rescale: $f(\omega_i) = \frac{\tilde{f}[(\omega_i - b)/a]}{\pi \sqrt{a^2 - (\omega_i - b)^2}}$	$f(z) = -\frac{1}{\pi} \operatorname{Im} \frac{\beta_0^2}{z - \alpha_0 - \frac{\beta_1^2}{z - \alpha_1 - \dots}}$ where $z = \omega_i + i\epsilon$
→ procedure is linear in $\mu_n$	→ procedure is non-linear in $\alpha_n, \beta_n$
→ well defined resolution $\propto 1/N$	→ $\epsilon$ is somewhat arbitrary

small advantage, but, of course, the application of the Hamiltonian as the dominant factor is the same for both methods. As a drawback, at high expansion order the Lanczos iteration tends to lose the orthogonality between the vectors  $|\phi_n\rangle$ , which it intends to establish by construction. When the Lanczos algorithm is applied to eigenvalue problems this loss of orthogonality usually signals the convergence of extremal eigenstates, and the algorithm then starts to generate artificial copies of the converged states (see Fig. 18.5). For the calculation of spectral densities or correlation functions this means that the information content of the  $\alpha_n$  and  $\beta_n$  does no longer increase proportionally to the number of iterations. Unfortunately, this deficiency can only be cured with more complex variants of the algorithm, which also increase the resource consumption. Chebyshev expansion is free from such defects, as there is a priori no orthogonality between the  $|\phi_n\rangle$ .

The reconstruction of the considered function from its moments  $\mu_n$  or coefficients  $\alpha_n, \beta_n$ , respectively, is also faster and simpler within the KPM, as it makes use of FFT. In addition, the KPM is a linear transformation of the moments  $\mu_n$ , a property we used extensively above when averaging moment data instead of the corresponding functions. Continued fractions, in contrast, are non-linear in the coefficients  $\alpha_n, \beta_n$ . A further advantage of KPM is our good understanding of its convergence and resolution as a function of the expansion order  $N$ . For the Lanczos algorithm these issues have not been worked out with the same rigor.

In Fig. 19.10 we compare KPM and Lanczos recursion, calculating the spectral function  $-\pi^{-1} \text{Im}\langle 0|c_{0\uparrow}(\omega - H)^{-1}c_{0\uparrow}^\dagger|0\rangle$  for the Hubbard model on a  $L = 12$  site ring and half-filling. With the Jackson kernel all features of the dynamical correlation function are resolved sharply, whereas with Lanczos recursion, by construction, we observe Lorentzian broadening. The Lanczos recursion data therefore is

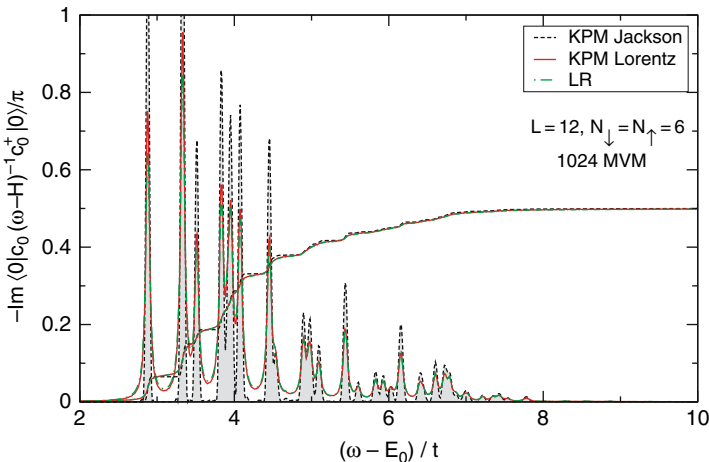


**Fig. 19.10.** The spectral function  $-\pi^{-1} \text{Im}\langle 0|c_{0\uparrow}(\omega - H)^{-1}c_{0\uparrow}^\dagger|0\rangle$  calculated for the Hubbard model with  $L = 12, N_\downarrow = N_\uparrow = 6$  using KPM and Lanczos recursion (LR). Lanczos recursion closely matches KPM with Lorentz kernel

comparable to KPM with Lorentz kernel, except that the calculation takes a little bit longer (about 10% in this simple case). Note also, that within KPM the calculation of non-diagonal correlation functions, like  $\langle 0|c_i(\omega - H)^{-1}c_j^\dagger|0\rangle$  with  $i \neq j$ , is much easier – see our discussion in Sect. 19.3.1.

In conclusion, we think that the Lanczos algorithm is an excellent tool for the calculation of extremal eigenstates of large sparse matrices, but for spectral densities and correlation functions the KPM (MEM) is the better choice. Of course, the advantages of both algorithms can be combined, e.g. when the Chebyshev expansion starts from an exact eigenstate that was calculated with the Lanczos algorithm.

## Acknowledgements

We would like to thank A. Alvermann, B. Bäuml, G. Hager, M. Hohenadler, E. Jeckelmann, M. Kinateter, G. Schubert, R.N. Silver, and G. Wellein for valuable discussions and technical support. This work was supported by Deutsche Forschungsgemeinschaft through SFB TR24 and SFB 512. Furthermore, we acknowledge generous computer granting by John von Neumann-Institut für Computing Jülich (NIC), Leibniz-Rechenzentrum München (LRZ) and Norddeutscher Verbund für Hoch- und Höchstleistungsrechnen (HLRN).

## References

1. A. Weiße, G. Wellein, A. Alvermann, H. Fehske, *Rev. Mod. Phys.* **78**, 275 (2006) 545, 551, 552, 569
2. R.N. Silver, H. Röder, *Int. J. Mod. Phys. C* **5**, 935 (1994) 546, 548, 555
3. J.P. Boyd, *Chebyshev and Fourier Spectral Methods*. No. 49 in *Lecture Notes in Engineering* (Springer-Verlag, Berlin, 1989) 546
4. M. Abramowitz, I.A. Stegun (eds.), *Handbook of Mathematical Functions with formulas, graphs, and mathematical tables* (Dover, New York, 1970) 546, 553
5. T.J. Rivlin, *Chebyshev polynomials: From Approximation Theory to Algebra and Number Theory*, 2nd edn. *Pure and Applied Mathematics* (John Wiley & Sons, New York, 1990) 546
6. E.W. Cheney, *Introduction to Approximation Theory* (McGraw-Hill, New York, 1966) 546
7. G.G. Lorentz, *Approximation of Functions* (Holt, Rinehart and Winston, New York, 1966) 546
8. C. Lanczos, *J. Res. Nat. Bur. Stand.* **45**, 255 (1950) 547, 572
9. J. Skilling, in *Maximum Entropy and Bayesian Methods*, ed. by J. Skilling (Kluwer, Dordrecht, 1988), *Fundamental Theories of Physics*, pp. 455–466 548, 555, 571
10. D.A. Drabold, O.F. Sankey, *Phys. Rev. Lett.* **70**, 3631 (1993) 548
11. L. Fejér, *Math. Ann.* **58**, 51 (1904) 551
12. D. Jackson, Über die Genauigkeit der Annäherung stetiger Funktionen durch ganze rationale Funktionen gegebenen Grades und trigonometrische Summen gegebener Ordnung. Ph.D. thesis, Georg-August-Universität Göttingen (1911) 551
13. D. Jackson, *T. Am. Math. Soc.* **13**, 491 (1912) 551

14. M. Frigo, S.G. Johnson, Proceedings of the IEEE **93**(2), 216 (2005). Special issue on “Program Generation, Optimization, and Platform Adaptation” 554
15. M. Frigo, S.G. Johnson. FFTW fast fourier transform library. URL <http://www.fftw.org/> 554
16. J.C. Wheeler, Phys. Rev. A **9**, 825 (1974) 555
17. R.N. Silver, H. Röder, A.F. Voter, D.J. Kress, J. Comput. Phys. **124**, 115 (1996) 555
18. P.W. Anderson, Phys. Rev. **109**, 1492 (1958) 556, 564
19. R. Abou-Chacra, D.J. Thouless, P.W. Anderson, J. Phys. C Solid State **6**, 1734 (1973) 556
20. R. Haydock, R.L. Te, Phys. Rev. B **49**, 10845 (1994) 556
21. V. Dobrosavljević, A.A. Pastor, B.K. Nikolić, Europhys. Lett. **62**, 76 (2003) 556
22. C.M. Soukoulis, Q. Li, G.S. Grest, Phys. Rev. B **45**, 7724 (1992) 556
23. S. Kirkpatrick, T.P. Eggarter, Phys. Rev. B **6**, 3598 (1972) 556
24. R. Berkovits, Y. Avishai, Phys. Rev. B **53**, R16125 (1996) 556
25. G. Schubert, A. Weiße, H. Fehske, Phys. Rev. B **71**, 045126 (2005) 557
26. K. Fabricius, B.M. McCoy, Phys. Rev. B **59**, 381 (1999) 559
27. C. Schindelin, H. Fehske, H. Büttner, D. Ihle, Phys. Rev. B **62**, 12141 (2000) 559
28. H. Fehske, C. Schindelin, A. Weiße, H. Büttner, D. Ihle, Braz. J. Phys. **30**, 720 (2000) 559
29. A. Weiße, H. Fehske, Phys. Rev. B **58**, 13526 (1998) 562
30. M. Hohenadler, G. Wellein, A.R. Bishop, A. Alvermann, H. Fehske, Phys. Rev. B **73**, 245120 (2006) 562
31. H. Fehske, E. Jeckelmann, in *Polarons in Bulk Materials and Systems With Reduced Dimensionality, International School of Physics Enrico Fermi*, Vol. 161, ed. by G. Iadonisi, J. Ranninger, G. De Filippis (IOS Press, Amsterdam, 2006), *International School of Physics Enrico Fermi*, Vol. 161, pp. 297–311 562
32. E. Jeckelmann, Phys. Rev. B **66**, 045114 (2002) 562, 569
33. A. Weiße, H. Fehske, G. Wellein, A.R. Bishop, Phys. Rev. B **62**, R747 (2000) 563
34. E. Jeckelmann, H. Fehske, in *Polarons in Bulk Materials and Systems With Reduced Dimensionality, International School of Physics Enrico Fermi*, Vol. 161, ed. by G. Iadonisi, J. Ranninger, G. De Filippis (IOS Press, Amsterdam, 2006), *International School of Physics Enrico Fermi*, Vol. 161, pp. 247–284 563
35. D.J. Thouless, Phys. Rep. **13**, 93 (1974) 565
36. P.A. Lee, T.V. Ramakrishnan, Rev. Mod. Phys. **57**, 287 (1985) 565
37. B. Kramer, A. Mac Kinnon, Rep. Prog. Phys. **56**, 1469 (1993) 565
38. A. Weiße, Eur. Phys. J. B **40**, 125 (2004) 565
39. H. Tal-Ezer, R. Kosloff, J. Chem. Phys. **81**, 3967 (1984) 566
40. J.B. Wang, T.T. Scholz, Phys. Rev. A **57**, 3554 (1998) 566
41. V.V. Dobrovitski, H. De Raedt, Phys. Rev. E **67**, 056702 (2003) 566
42. W.H. Press, S.A. Teukolsky, W.T. Vetterling, B.P. Flannery, *Numerical Recipes in C: The Art of Scientific Computing*, 2nd edn. (Cambridge University Press, Cambridge, 1992) 567
43. J. Bonča, S.A. Trugman, I. Batistić, Phys. Rev. B **60**, 1633 (1999) 567, 569
44. S.A. Trugman, L.C. Ku, J. Bonča, J. Supercond. **17**, 193 (2004) 567
45. H. Fehske and S.A. Trugman in *Polarons in Advanced Materials*, Ed. A.S. Alexandrov, Springer Series in Material Sciences Vol. 103, pp. 393–461 (Canopus/Springer, Dordrecht 2007) 568
46. C. Gros, R. Valentí, Ann. Phys. (Leipzig) **3**, 460 (1994) 568
47. D. Sénéchal, D. Perez, M. Pioro-Ladrière, Phys. Rev. Lett. **84**, 522 (2000) 568, 571
48. D. Sénéchal, D. Perez, D. Plouffe, Phys. Rev. B **66**, 075129 (2002) 568
49. S.R. White, Phys. Rev. Lett. **69**, 2863 (1992) 569
50. F.H.L. Essler, H. Frahm, F. Göhmann, A. Klümper, V.E. Korepin, *The One-Dimensional Hubbard Model* (Cambridge University Press, Cambridge, 2005) 570

51. E. Jeckelmann, F. Gebhard, F.H.L. Essler, Phys. Rev. Lett. **85**, 3910 (2000) 570
52. L.R. Mead, N. Papanicolaou, J. Math. Phys. **25**, 2404 (1984) 571
53. I. Turek, J. Phys. C Solid State **21**, 3251 (1988) 571
54. R.N. Silver, H. Röder, Phys. Rev. E **56**, 4822 (1997) 571, 572
55. K. Bandyopadhyay, A.K. Bhattacharya, P. Biswas, D.A. Drabold, Phys. Rev. E **71**, 057701 (2005) 571
56. B. Bäuml, G. Wellein, H. Fehske, Phys. Rev. B **58**, 3663 (1998) 572
57. E. Dagotto, Rev. Mod. Phys. **66**, 763 (1994) 572
58. J.K. Cullum, R.A. Willoughby, *Lanczos Algorithms for Large Symmetric Eigenvalue Computations*, Vol. I & II (Birkhäuser, Boston, 1985) 572
59. R. Haydock, V. Heine, M.J. Kelly, J. Phys. C Solid State **5**, 2845 (1972) 572
60. R. Haydock, V. Heine, M.J. Kelly, J. Phys. C Solid State **8**, 2591 (1975) 572
61. P. Lambin, J.P. Gaspard, Phys. Rev. B **26**, 4356 (1982) 572
62. C. Benoit, E. Royer, G. Poussigue, J. Phys. Cond. Mat. **4**, 3125 (1992) 572
63. E. Gagliano, C. Balseiro, Phys. Rev. Lett. **59**, 2999 (1987) 572
64. Q. Zhong, S. Sorella, A. Parola, Phys. Rev. B **49**, 6408 (1994) 572
65. J. Jaklič, P. Prelovšek, Phys. Rev. B **49**, 5065 (1994) 573
66. J. Jaklič, P. Prelovšek, Adv. Phys. **49**, 1 (2000) 573
67. M. Aichhorn, M. Daghofer, H.G. Evertz, W. von der Linden, Phys. Rev. B **67**, 161103 (2003) 573
68. M.W. Long, P. Prelovšek, S. El Shawish, J. Karadamoglou, X. Zotos, Phys. Rev. B **68**, 235106 (2003) 573